Why are Mountaintops Cold? The Transition of Surface Lapse Rate on Dry Planets

Bowen Fan[1], Malte F. Jansen[1], Michael A. Mischna[2], Edwin S. Kite[1]

[1]Department of the Geophysical Sciences, University of Chicago, Chicago, IL, 60637, USA
[2]Jet Propulsion Laboratory, California Institute of Technology, Pasadena, CA, 91109, USA

Key Points:

- Surface lapse rate robustly increases with atmospheric longwave optical thickness (greenhouse effect) in a general circulation model.
- Increased pressure further contributes to a tropical surface lapse rate increase in moderately opaque atmospheres.
- A simple model, assuming weak temperature gradient and highland convective adjustment, provides insight into the mechanisms.

Corresponding author: Bowen Fan, bowen27@uchicago.edu

Abstract

Understanding surface temperature is important for habitability. Recent work on Mars has found that the dependence of surface temperature on elevation (surface lapse rate) converges to zero in the limit of a thin CO_2 atmosphere. However, the mechanisms that control the surface lapse rate are still not fully understood. It remains unclear how the surface lapse rate depends on both greenhouse effect and surface pressure. Here, we use climate models to study when and why "mountaintops are cold". We find the tropical surface lapse rate increases with the greenhouse effect and with surface pressure. The greenhouse effect dominates the surface lapse rate transition and is robust across latitudes. The pressure effect is important at low latitudes in moderately opaque ($\tau \sim 0.1$) atmospheres. A simple model provides insights into the mechanisms of the transition. Our results suggest that topographic cold-trapping may be important for the climate of arid planets.

Plain Language Summary

Understanding surface temperature on a planet is important for life on Earth and beyond. On Earth, we know "mountaintops are cold", which means that surface temperature decreases with elevation. However, this idea does not apply on Mars. Here, we investigate when and why the Earth-based understanding holds for planets with different types of atmospheres. Using a global climate model, we show that both the greenhouse effect (atmospheric infrared opacity) and the pressure effect (atmospheric thickness) are important. The weaker the greenhouse effect, or the thinner the atmosphere, the slower the surface cools with elevation. The greenhouse effect plays the dominant role, but in moderately opaque atmospheres, the pressure effect becomes important as well. Our work reveals a novel connection between climate and geomorphology. For example, on a planet with a pure O_2 atmosphere, we do not expect that "mountaintops are cold".

1 Introduction

Surface temperature, T_s, is fundamental for understanding habitability (Seager, 2013). In addition to the direct implications of surface temperature for life, the distribution of surface temperature defines the cold trap (where moisture tends to condense and accumulate), which regulates the hydrological cycle on an arid planet (Mitchell & Lora, 2016; Ding & Wordsworth, 2020).

There are two paradigms for estimating the distribution of surface temperature. The first paradigm, which we refer to as "radiation deficits are cold", states that the coldest region is close to the time-mean minimum of solar radiation. These regions are the deficits of net radiation flux at the top of the atmosphere. For example, the poles are regions of radiation deficit for Earth and modern Mars, the night hemisphere is the region of radiation deficit for synchronously rotating exoplanets (Wordsworth, 2015), and the tropics were the region of radiation deficit for pre-modern Mars at times when the obliquity was very high (Forget et al., 2006). This paradigm focuses on the large-scale pattern of surface temperature, and has been extensively studied (e.g., Held, 1993; Forget et al., 2006; Kaspi & Showman, 2015; Wordsworth, 2015).

The second paradigm, which we refer to as "mountaintops are cold," emphasizes local processes and emerged long before the modern era. This paradigm states that the change of surface temperature with elevation should follow that of the atmosphere, which can be quantified as the lapse rate. For a well-mixed, isolated atmospheric column without condensible species, the lapse rate is the dry adiabat, Γ_{ad}:

$$\Gamma_{ad} = -\frac{dT_a}{dZ} = \frac{g}{c_p} \tag{1}$$

where T_a is atmospheric temperature, Z is height, g is gravity, and c_p is the specific heat of air. If surface temperature also follows this adiabatic lapse rate, we therefore expect colder temperature at higher elevations. Taken together, these two paradigms predict how surface temperature changes horizontally (by solar radiation) and following surface elevation (by gravity and atmospheric composition).

However, the idea that "mountaintops are cold" does not apply to Mars. Surface lapse rate, Γ_s, (the change of surface temperature with elevation) is weak on modern Mars (Sagan & Pollack, 1968). Recent work on early Mars has linked the Martian surface lapse rate to the atmosphere's evolution (Forget et al., 2013; Wordsworth et al., 2013; Wordsworth, 2016; Kite, 2019). Specifically, Γ_s is close to Γ_{ad} only for scenarios with thick CO_2 atmospheres. For thin CO_2 atmospheres, Γ_s is close to zero. From the perspective of surface energy budgets, Forget et al. (2013) and Wordsworth (2016) suggested that both the sensible heat flux, SH, and atmospheric longwave heating, LW_a, are important in modulating T_s when the CO_2 atmosphere goes from thick to thin. However, the mechanisms that control the transition in Γ_s are not fully understood. It remains unclear whether SH or LW_a is more important for the change of Γ_s seen in earlier work, and what controls the changes in SH and LW_a. Relatedly, it is not clear in how far the surface lapse rate is sensitive primarily to the change in the surface pressure, versus the change in the greenhouse effect. While the surface pressure and greenhouse effect are directly linked in a pure CO_2 atmosphere, understanding the role of these two distinct effects is important to predict the surface lapse rate on planets with different atmospheres. Are mountaintops still cold for planets with, for example, a thick, pure O_2 atmosphere (high pressure, no greenhouse effect)? What about a thin, fluoride atmosphere (e.g., CF_4 or SF_6, low pressure, strong greenhouse effect), as suggested by Marinova et al. (2005)?

In this paper, we seek a better understanding of when and why "mountaintops are cold", for planets with different greenhouse gas forcings and atmospheric pressures. Following Koll and Abbot (2016), we focus on "dry planets" (idealized planets forced by gray radiation) to gain a basic understanding of the phenomenon. We introduce our methodology in Section 2. We present and analyse the results in Section 3. Section 4 includes our conclusion, limitations of this research, and implications for future work on different planets.

2 Methods

2.1 General Circulation Model (GCM)

We use the MarsWRF GCM (Richardson et al., 2007; Toigo et al., 2012) to investigate temperature distribution across different atmospheres. The model resolution is $72\times36\times40$ gridpoints in longitude/latitude/height. All simulations are run for 20 years with 5 years of spin up and averages taken over the last 15 years.

To aid understanding, we use idealized simulations with the following settings. The radiative transfer is computed using a gray gas scheme. Under the scheme, the longwave absorption coefficient, κ, is varied, allowing us to decouple the greenhouse effect from surface pressure. The shortwave Rayleigh scattering and absorption are set to zero. Surface albedo is uniformly zero. We also carry out simulations with a pure CO_2 atmosphere, using a correlated-k scheme for radiative transfer (Mischna et al., 2012) to validate our simulations against earlier studies (Supplementary Information A).

For the default simulations, the planetary obliquity and orbital eccentricity are set to zero, with solar constant 75% of the modern Martian value, representing the faint young Sun. Diurnal cycles are disabled. Planetary size and rotation rate are set to Mars values. We explore different planetary climates over a 2D parameter space: varying mean surface

pressure, p_s, and mean surface longwave optical depth, τ, between 0.01 bar and 5 bar[1] and between 0.003 and 5, respectively. The range of values is chosen so as to compare with earlier work (Forget et al., 2013; Kamada et al., 2021). We note that higher values of p_s or τ lead to an energy flux imbalance at the top of the atmosphere ($> 5\%$ imbalance compared to the net shortwave flux) in MarsWRF. Our simulations are performed with an idealized topography, which is a Gaussian-shaped mountain placed at the equator (blue dashed contours in Fig. 1a & Fig. 1b):

$$Z_s = 6000 \times e^{-\frac{1}{2}\frac{X^2}{9^2}} \times e^{-\frac{1}{2}\frac{Y^2}{7^2}} \tag{2}$$

where Z_s is surface elevation (in meters), and X and Y are longitude and latitude grid points ($-35.5 \leq X \leq 35.5$, $-17.5 \leq Y \leq 17.5$), respectively.

The surface sensible heat flux is given by:

$$SH = \rho c_p C_h U^* (\theta_a - \theta_s) \tag{3}$$

where ρ is near-surface air density, c_p is the specific heat capacity of air, C_h is a heat exchange coefficient, U^* is friction velocity, θ_a is near-surface potential temperature, and θ_s is surface potential temperature, respectively. Both C_h and U^* are calculated inside MarsWRF's surface layer scheme (Zhang & Anthes, 1982), which uses Monin-Obukhov similarity and accounts for four stability categories: stable, mechanically induced turbulence, unstable forced convection, and unstable free convection.

To connect our idealized simulations to more Mars-relevant scenarios, we perform the following sensitivity tests: (1) obliquity set to 20°; (2) obliquity set to 20° and with condensation and sublimation of ice caps (Chow et al., 2019) (no atmospheric collapse is found in this case); and (3) modern Mars topography. For each set of sensitivity tests, we vary τ while fixing p_s to 1 bar, and we vary p_s and while fixing τ to 0.1.

We also perform two sets of mechanism-denial experiments to verify the role of sensible heat flux, SH, as well as the role of atmospheric mass in modulating SH. In the first set of mechanism-denial experiments, SH is forced to be 0. In the second set of mechanism-denial experiments, the value of ρ in Eq. (3) is held fixed at the reference value for a 1-bar atmosphere, thereby eliminating the direct effect of surface pressure on the surface turbulent heat flux. The effect of varying atmospheric mass is still considered in all other components of the model, and SH is allowed to change as a result of indirect effects.

2.2 Definition of the orographic temperature control: relative surface lapse rate, γ

The relationship between surface temperature, T_s, and elevation, Z_s, is quantified via the surface lapse rate, Γ_s:

$$\Gamma_s = -\frac{dT_s}{dZ_s} \tag{4}$$

where dT_s/dZ_s is quantified by calculating a linear regression of the time-mean model output in the tropical belt 20° N - 20° S (see the red dashed lines in Fig. 1a and white dashed lines in Fig. 1b). We also analyzed the effect of topography in the mid-latitudes (Supplementary Information B) to test the sensitivity to the choice of latitude.

Furthermore, we define the relative surface lapse rate, γ, as the surface lapse rate scaled by the atmospheric dry adiabat:

[1] MarsWRF requires p_s to be multiples of modern Mars pressure (610 Pa). Here we choose the multiplier to be 2, 17, 167, 833, which correspond to p_s being 0.012, 0.103, 1.02, 5.08 bar.

$$\gamma = \frac{\Gamma_s}{\Gamma_a} \times 100\% \tag{5}$$

Thus we expect, for the Earth-like regime ("mountaintops are cold"), γ to be close to 100%.

3 Results

3.1 The transition of surface lapse rate

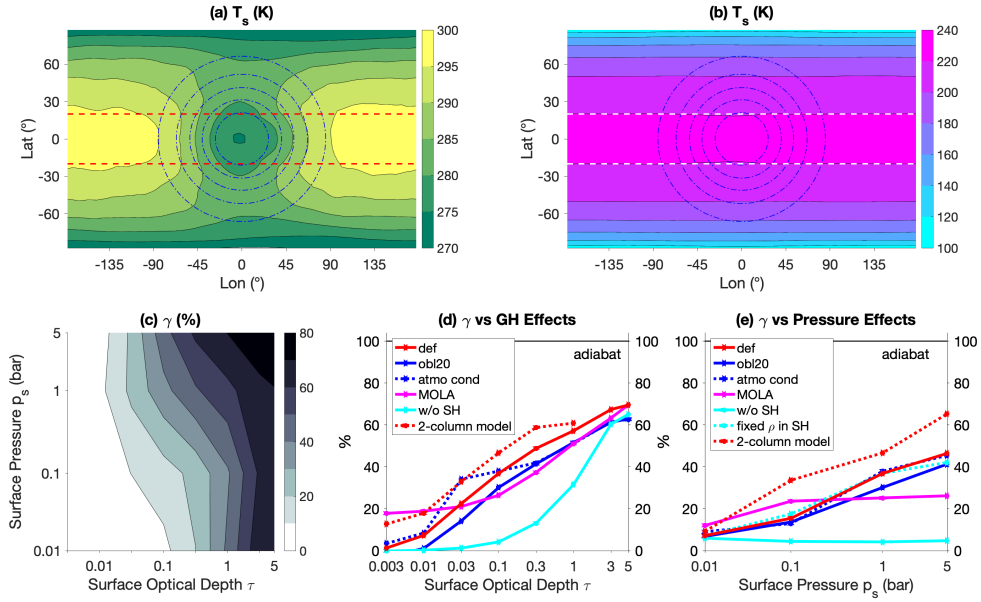

Figure 1. (a) Surface temperature T_s (filled contours) for surface pressure $p_s = 5$ bar and global mean surface optical depth $\tau = 5$. The topography is plotted in blue dashed lines with a contour interval of 1000 m from 1000 m to 5000 m. The horizontal red dashed lines indicate the zone for tropical averaging (see Section 2.2). (b) Same as (a), but for the case with $p_s = 0.01$ bar and $\tau = 0.01$. The horizontal white dashed lines indicate the tropical averaging zone. (c) Relative surface lapse rate, γ (defined in Eq. 5), as a function of greenhouse effect, τ, and atmospheric thickness, p_s. The data is sampled on a log-scale grid with $\tau = 0.003, 0.01, 0.1, 0.3, 1, 3, 5$ and $p_s = 0.01, 0.1, 1, 5$ bar. (d) The dependence of γ on τ when $p_s = 1$ bar. Red solid (def): default simulation, obliquity equals zero, no atmospheric condensation, idealized topography, sensible heat flux enabled. Blue solid (obl20): as def, but with obliquity set to 20°. Blue dotted (atmo cond): as def, but with obliquity set to 20°, and a CO_2-like atmospheric condensation is enabled. Magenta (MOLA): as def, but with Mars Orbiter Laser Altimeter topography. Cyan solid (w/o SH): as def, but with sensible heat flux disabled. Red dotted (2-column model): calculations from the simple two-column model (see Section 3.4). (e) As (d), but with varying p_s and fixed $\tau = 0.1$. Cyan dotted (fixed ρ in SH): as def, but the value of air density, ρ, is held fixed at the reference value for a 1-bar atmosphere in Eq. (3).

We first examine the horizontal distribution of temperature in our GCM simulations. Fig. 1a&1b show the typical annual mean surface temperature, T_s, in different climates. In all simulations, T_s decreases with increasing latitude. This is consistent with our default setting of obliquity to 0° (polar cold traps are created by radiation deficits). The pattern

of near-surface atmospheric temperature, T_a, follows T_s closely (Supplementary Information C), with minor modulation by the winds across the elevated topography (Wordsworth et al., 2015).

For the topographic control on surface temperature, we find two opposing limits for thick and thin atmospheres. In the thick atmosphere limit ($p_s = 5$ bar, $\tau = 5$), we find "mountaintops are cold" (Fig. 1a): T_s decreases with Z_s ($\gamma \to 100\%$). In the thin atmosphere limit ($p_s = 0.01$ bar, $\tau = 0.01$), the T_s distribution becomes zonally banded (Fig. 1b), with almost no dependence on topography ($\gamma \to 0$).

The transition of the tropical surface temperature distribution across different climates can be quantified as the change in the relative surface lapse rate, γ, with varying surface longwave optical depth, τ, and surface pressure, p_s (Fig. 1c). We find γ increases with τ and p_s. However, the role of the greenhouse effect (i.e., variations in τ) and the pressure effect (variations in p_s) are not symmetric. Within our parameter space, we find γ always increases significantly with τ for any given p_s, but γ increases significantly with p_s only for intermediate values of τ ($\tau \sim 0.1$). When $\tau \leq 0.01$, we find $\gamma \approx 0$ for all values of p_s. When $\tau > 1$, γ is close to saturation and increases only slowly with p_s. Sensitivity of γ on p_s is smaller than that on τ even at intermediate τ. For example, starting from $\tau = 0.1$, $p_s = 1$ bar (i.e., a cold early Mars), decreasing τ by one order of magnitude leads to γ decreasing from 37% to 7% (red solid line in Fig. 1d), while decreasing p_s by one order of magnitude leads to γ decreasing from 37% to 15% (red solid line in Fig. 1e).

We also explore the change of γ with τ and p_s in sensitivity tests. Here we focus on Mars-relevant scenarios when the obliquity is non-zero, atmospheric condensation occurs, or the topography is different. We find γ is slightly smaller, but still increases with τ and p_s, when the obliquity is non-zero (compare the blue solid line to the red solid line in Fig. 1d&1e). The relationship between γ and τ and p_s also holds when the atmosphere partially condenses and sublimates seasonally (blue dotted lines in Fig. 1d&1e). Changing to Mars topography decreases the sensitivity of γ on τ and, in particular, p_s, although the qualitative results remain robust (magenta lines in Fig. 1d&1e, also see Supplementary Information A). Especially, the p_s sensitivity becomes very small. The surface lapse rate in the mid-latitudes (discussed in Supplementary Information B)) also shows similar sensitivity to τ, but is virtually insensitive to p_s. In conclusion, we confirm that both the greenhouse effect and the pressure effect can contribute to the lapse rate transition, as suggested by earlier studies (Forget et al., 2013; Wordsworth, 2016), but the greenhouse effect dominates and is more robust.

3.2 Surface energy budgets

How do the longwave optical depth and surface pressure control the surface lapse rate in different climates? Wordsworth (2016) proposed using the surface energy budget to understand the mechanisms controlling the surface lapse rate. The surface energy budget is:

$$SW + LW_a = LW_s + SH \tag{6}$$

where SW is the net shortwave heating from the star, LW_a is the longwave heating from the atmosphere (greenhouse effect), and LW_s is the longwave cooling by surface emission, which is directly related to T_s:

$$LW_s = \sigma T_s^4 \tag{7}$$

where $\sigma = 5.67 \times 10^{-8}$ W/m^2/K^4 is the Stefan-Boltzmann constant. SH is the sensible heat flux. There is no latent heat term in the surface energy budget because water vapor and CO_2 condensation are disabled in our default simulations.

To better understand the role of atmospheric optical thickness and pressure on the surface temperature structure, we analyze the surface energy budget in our simulations with varying τ and p_s. To visualize the model output, we apply a tropical meridional average (20° N - 20° S) and time-average to the model output. With this approach, the temperature gradient due to solar insolation is minimized. The annual mean longitudinal variation in T_s corresponds to the LW_s term (see Eq. 7). For example, the red line in Fig. 2c indicates a temperature minimum at longitude = 0° in the tropics, which corresponds to the highland in our idealized topography (Fig. 1a).

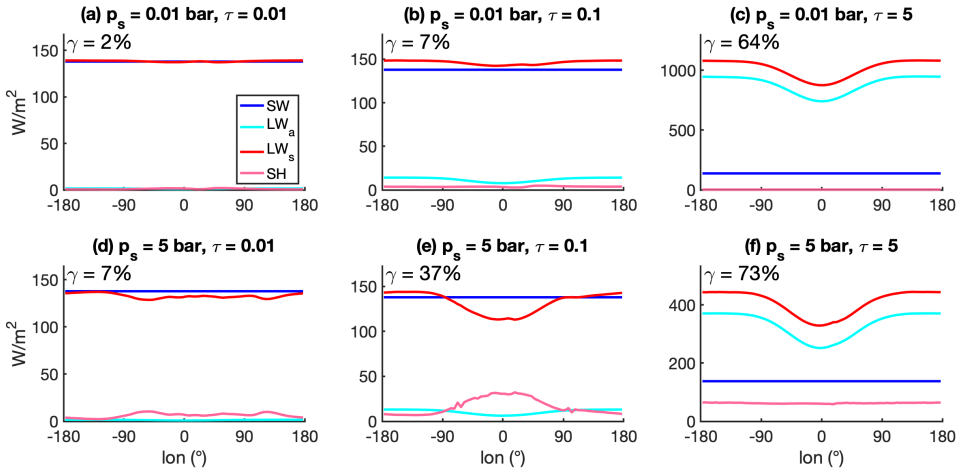

Figure 2. Time-averaged surface energy budgets for typical scenarios: (a) $p_s = 0.01$ bar, $\tau = 0.01$, (b) $p_s = 0.01$ bar, $\tau = 0.1$, (c) $p_s = 0.01$ bar, $\tau = 5$, (d) $p_s = 5$ bar, $\tau = 0.01$, (e) $p_s = 5$ bar, $\tau = 0.1$, (f) $p_s = 5$ bar, $\tau = 5$. Relative surface lapse rate (surface lapse rate scaled by adiabat), γ, for each case is indicated in the upper-left corner. SW is the net shortwave heating from the star, LW_a is the longwave heating from the greenhouse effect, LW_s is the longwave cooling by surface emission, and SH is the cooling by sensible heat flux, respectively. Each term is meridionally averaged within the tropics (20°N - 20°S). A dip in the red curve indicates a correlation between T_s and topography (lower T_s, thus lower emission over the highlands - see Eq. 7).

We find three typical scenarios for the zonal structure of the tropical surface energy budget (Fig. 2, see Supplementary Information D for all cases). For an atmosphere that is optically transparent ($\tau < 0.1$, Fig. 2a&2d), or thin and optically intermediate ($p_s \leq 0.1$ bar, $\tau \sim 0.1$, Fig. 2b), the major balance is between surface emission (LW_s, red lines) and shortwave absorption (SW, blue lines). The other terms are small. Since SW does not vary with topographic elevation in our model setup, LW_s (and thus T_s) can't vary much either. Hence, γ is close to zero under this scenario. For optically thick atmospheres ($\tau \geq 1$, Fig. 2c&2f), the dominant balance is between surface emission, LW_s, and longwave heating (LW_a, cyan lines). The longwave heating is weaker over the highlands compared to the lowlands, thus the highland surface is colder. Although the magnitude of SH is non-negligible for massive atmospheres ($p_s \leq 1$ bar), the spatial variations of SH are small under this scenario. This is consistent with our earlier results that γ is dominated by τ when $\tau \geq 1$ (Fig. 1c). For massive, moderately opaque atmospheres ($p_s \geq 1$ bar, $\tau \sim 0.1$, Fig. 1e), SH variations are large enough to generate a significant pattern in LW_s (and thence T_s), while LW_a is still small. Therefore, in this regime, variations in SH are important for the surface lapse rate.

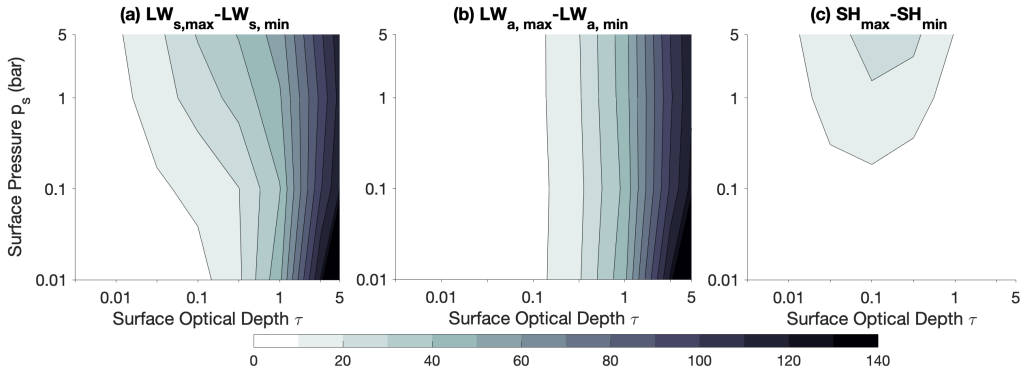

Figure 3. Time-averaged surface energy budgets (unit in W/m^2) for all cases in Fig. 1c. Same as Fig. 2, each variable is meridionally averaged within the tropics (20°N - 20°S). (a) Contrast of surface emission, LW_s, (b) contrast of greenhouse effect, LW_a, (c) contrast of sensible heat flux, SH.

To illustrate the role of spatial variations in the longwave radiation and surface heat flux across the full parameter regime, Fig. 3 shows the highland-lowland contrast as a function of τ and p_s in our default simulations. Here, we focus on the difference between the maximum and minimum values (positive-definite) to visualize the highland-lowland contrast. By definition, the change in surface emission contrast (Fig. 3a) reflects the surface lapse rate transition (Fig. 1c). The surface emission contrast $LW_{s,max} - LW_{s,min}$ can be decomposed into the contribution from the greenhouse forcing, LW_a, and sensible heat flux, SH. As expected, the change in LW_a follows τ and dominates the transition (Fig. 3b). The SH contrast additionally modulates the LW_s contrast when the atmosphere is moderately opaque (Fig. 3c).

Wordsworth (2016) proposed that p_s affects γ by modulating ρ in the equation of SH (Eq. 3). To test the importance of SH in general, and the role of ρ in the surface heat exchange equation in particular, we perform two sets of mechanism-denial experiments with modified SH. In the first set of simulations, we manually disable SH, which significantly reduces γ when the atmosphere is intermediately opaque ($\tau \sim 0.1$), such that γ remains small at all surface pressures (solid cyan lines in Fig. 1d&1e). However, γ still becomes large for very large τ. In the second set of simulations, we fix ρ at the reference value for a 1-bar atmosphere in the equation for SH (Eq. 3), which does not significantly change the sensitivity of γ to p_s (dotted cyan line in Fig. 1e). Thus, SH is necessary for the increase of γ with p_s at intermediate τ, but the increase of ρ in Eq. (3) is not the primary mechanism.

3.3 Surface lapse rate transition in a two-column model

To improve our understanding of the mechanisms that cause the surface lapse-rate transition, we construct a simpler two-column model, building on previous work by Yang and Abbot (2014), Wordsworth (2015), and Koll and Abbot (2016). Similar to Yang and Abbot (2014), our model is formulated by requiring energy balance in the free troposphere and at the surface (Eq. 8 - Eq. 11), making the Weak Temperature Gradient (WTG) approximation (Eq. 12), and enforcing convective stability or neutrality (Eq. 13 - Eq. 14). The model is therefore built on the hypothesis that the key ingredients to explain the surface lapse rate include 1) a WTG in the free troposphere, 2) convection, which maintains an adiabatic lapse-rate if and only if the radiative-advective equilibrium solution is unstable, and 3) radiative-advective equilibrium (i.e. negligible turbulent heat flux) when the solution is stable. The model equations are:

$$SW - F_{c,HL} + \epsilon_H L\sigma T_{a,HL}^4 - \sigma T_{s,HL}^4 = 0 \tag{8}$$

$$F_{c,HL} - F_a - F_H + \epsilon_{HL}\sigma T_{s,HL}^4 - 2\epsilon_{HL}\sigma T_{a,HL}^4 = 0 \tag{9}$$

$$F_{c,LL} + \frac{\alpha}{1-\alpha}F_a - F_H + \epsilon_{LL}\sigma T_{s,LL}^4 - 2\epsilon_{LL}\sigma T_{a,LL}^4 = 0 \tag{10}$$

$$SW - F_{c,LL} + \epsilon_{LL}\sigma T_{a,LL}^4 - \sigma T_{s,LL}^4 = 0 \tag{11}$$

$$T_{a,HL} - T_{a,LL} = 0 \tag{12}$$

$$DSE_{s,HL}\begin{cases} = DSE_{a,HL} & \text{convective highland, solve for } F_{c,HL} \\ < DSE_{a,HL} & \text{stratified highland, } F_{c,HL} = 0 \end{cases} \tag{13}$$

$$DSE_{s,LL}\begin{cases} = DSE_{a,LL} & \text{convective lowland, solve for } F_{c,LL} \\ < DSE_{a,LL} & \text{stratified lowland, } F_{c,LL} = 0 \end{cases} \tag{14}$$

Here, $T_{s,HL}$ and $T_{s,LL}$ are the surface temperatures of the highland and lowland, respectively; $T_{a,HL}$ and $T_{a,LL}$ are the free-tropospheric temperature of the highland and lowland, respectively; $F_{c,HL}$ and $F_{c,LL}$ are the convective heat flux from the surface to the free troposphere in the highland and lowland column, respectively; F_a represents atmospheric heat transport between the columns; F_H represents the atmospheric heat outflow from the tropical band caused by the Hadley circulation; α is the surface area fraction of the highland within the latitudinal belt; ϵ_{HL} and ϵ_{LL} are the atmospheric emissivities of the two columns; and DSE is the dry static energy at the respective location. The values of ϵ and DSE are calculated as:

$$\epsilon_{HL} = \frac{p_{s,HL}}{p_s}\tau \tag{15}$$

$$\epsilon_{LL} = \frac{p_{s,LL}}{p_s}\tau \tag{16}$$

$$DSE_i = c_p T_i + gZ_i \tag{17}$$

The choices of parameters are explained in Supplementary Information E. Using the seven equations (8)-(14), we numerically determine solutions for the seven dependent variables of the model: surface temperature ($T_{s,HL}$ and $T_{s,LL}$), atmospheric temperature ($T_{a,HL}$ and $T_{a,LL}$), atmospheric heat transport between the columns F_a, and convective heat flux ($F_{c,HL}$ and $F_{c,LL}$). We note that the model can be further simplified by combining Eq. (9), (10) and (12) into a single equation to eliminate F_a and merge $T_{a,HL}$ and $T_{a,LL}$ into a single unknown ($T_{a,HL} = T_{a,LL} \equiv T_a$). Moreover, since convection is never active in the lowland for any of the presented solutions, we can obtain the same results by setting $F_{c,LL} = 0$ and eliminating Eq. (14). However, we found that these simplifications provide no additional insight, and numerical solution is trivial with either formulation. Similar to Wordsworth (2015), our model is constructed for cases when $\tau \ll 1$. For optically thick atmospheres ($\tau > 1$), the surface is no longer radiatively heated by the same atmospheric layer that emits to space, thus the single-layer-atmosphere approximation breaks down.

The two-column model is capable of reproducing the increase of γ with τ and p_s (red dotted lines, Fig. 1d&1e). From the surface energy budget perspective, our two-column model is qualitatively consistent with the transitions in the highland-lowland contrast from the GCM (Supplementary Information E).

In addition to confirming that the assumptions entering the two-column model formulation appear to be sufficient to understand the lapse rate transition, the model provides some insight into the specific mechanisms. The surface energy budget analysis discussed above showed that differential longwave radiation between the lowland and highland is important to understand the surface lapse rate at high optical thickness. A naive interpretation is that LW_a is smaller over the highland simply because the overlying atmosphere is less massive

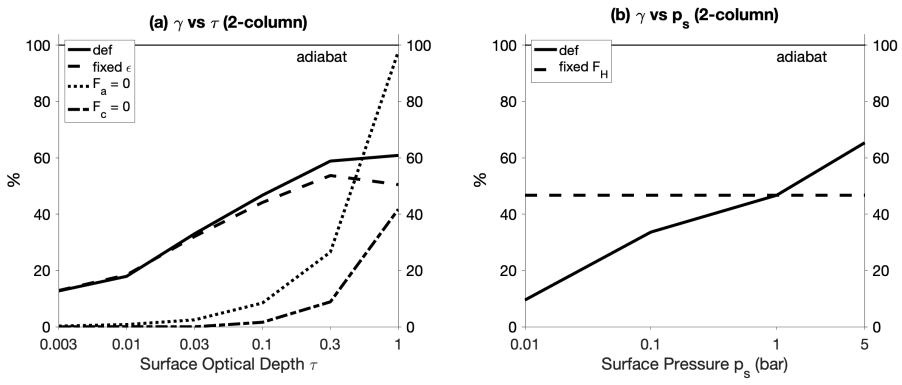

Figure 4. The transition of relative lapse rate, γ, in the two-column model. (a) The dependence of γ on the greenhouse effect, τ. Solid line (def): default case - same as the red dotted line in Fig. 1d. Dashed line (fixed ϵ): the case with uniform greenhouse forcing above highlands and lowlands. Dotted line ($F_a = 0$): the case with no heat advection between the highland and lowland atmosphere. Dash-dotted line ($F_c = 0$): the case with no convection between the atmosphere and surface. (b) The dependence of γ on the pressure effect. Solid line (def): default case - same as the red dotted line in Fig. 1e. Dashed line (fixed F_H): the case with meridional heat advection fixed to the 1 bar value ($F_H = 6.5528$ W/m^2).

and hence has a weaker greenhouse effect. We can test this hypothesis in the two column model by eliminating the difference in ϵ between the two columns (setting $\frac{p_{s,HL}}{p_s} = \frac{p_{s,LL}}{p_s} = 1$ in Eq. 15&16). We find the change of γ with τ persists in this sensitivity experiment, and indeed is only weakly affected (compare solid and dashed lines in Fig. 4a).

So what instead explains the transition with τ? In the two-column model, the increase of the surface lapse rate, γ, is directly related to the lapse rate in the lowland column, due to the assumption of WTG in the atmosphere and convective adjustment over the highlands. The importance of these two assumptions can be illustrated by setting either F_a or F_c to zero (by modifying Eq. 12 or Eq. 13), which changes the relationship between γ and τ significantly (dotted line and dash-dotted line in Fig. 4a). Notably, without convective heat transport between the surface and atmosphere, the sensitivity of γ effectively reproduces the GCM simulations without SH (solid cyan line in Fig. 1d). WTG and convective adjustment link the surface lapse rate to the lowland atmospheric lapse rate, which, in turn, is governed by radiative-advective equilibrium. As discussed in Payne et al. (2015) and Cronin and Jansen (2016), the lapse rate of a column in radiative-advective equilibrium increases under increasing greenhouse forcing, as the increased radiative flux cools the atmosphere and heats the surface.

In the next step we examine the sensitivity to the global mean surface pressure, p_s. In the two-column model, p_s, by construction, affects the solution only via its indirect effect on the meridional heat transport F_H, which is here diagnosed from the GCM simulations. The sensible heat flux, SH, which in the real world is associated with complex boundary layer physics (Joshi et al., 2020), is implied by Eq. 13&14. Consistent with Kaspi and Showman (2015), we find that higher p_s (and thus greater atmospheric mass) drives larger F_H. Following our argument above, atmospheric heat flux divergence from the tropics, F_H, leads to a reduction of the net atmospheric heat flux convergence over the lowlands, which leads to a reduction in the atmospheric lapse rate (and, hence, a reduction in the surface lapse rate, γ). The mechanism can be illustrated by fixing F_H. As expected, we find that when F_H is fixed, the sensitivity of γ to p_s disappears (Fig. 4b).

Taken together with the GCM simulations, the results suggest that both a weak temperature gradient and highland convection are important for explaining the sensitivity of γ to the greenhouse effect and pressure effect. Meanwhile, the spatial variations in the column-integrated greenhouse gas and the near-surface air density do not play a major role in the sensitivity of the surface lapse rate.

4 Discussion and Summary

"Radiation deficits are cold" and "mountaintops are cold" comprise the usual expectation for the distribution of surface temperature, T_s. Here, using a GCM simulating a fast-rotating, dry planet, we argue that whether "mountaintops are cold" depends on both the greenhouse effect (longwave optical depth, τ) and surface pressure, p_s. Specifically, the dependence of T_s on surface elevation is quantified as the tropical surface lapse rate relative to the adiabat, γ. We find that γ increases with τ and p_s. However, the roles of the greenhouse effect and pressure effect are not symmetric. At all surface pressures, we find that γ is close to zero for very small τ, and approaches 100% as $\tau > 1$. Surface pressure plays a significant role at intermediate τ, where more massive atmospheres tend to have larger γ in the tropics, but the effect of p_s is less robust. From a surface energy budget perspective, spatial variations in the downwelling atmospheric longwave radiation LW_a are responsible for the topographic surface temperature variations for optically thick atmospheres ($\tau > 1$), while for optically moderate atmospheres ($\tau \sim 0.1$) surface temperature variations (and the associated variations in surface longwave emission LW_s) are maintained by variations in the sensible heat flux, SH. Large γ requires a weak temperature gradient in the atmosphere and effective coupling between the surface and the atmospheric temperature, where the coupling can occur either radiatively or via SH. The surface lapse rate transition can be reproduced in a two-column, two-layer model, consisting of a convective highland column together with a stable lowland column, coupled via the weak temperature gradient assumption in the atmosphere. The two-column model suggests that weak temperature gradient and highland convection are important to explain the lapse rate transition. Increases in optical thickness or surface pressure then affect the tropical surface lapse rate by destabilizing the atmospheric lapse rate over the lowlands.

This paper focuses on the surface temperature distribution on fast-rotating, dry planets. We can speculate how the conclusions might differ on other planets, although future work should use GCMs to verify these predictions. (1) For tidally locked planets, solar insolation never reaches the permanent night hemisphere, such that the nightside, heated by advection, is stably stratified (Joshi et al., 2020; Ding & Wordsworth, 2021). Thus, the mountaintops in the night hemisphere might be warm depending on the strength of the thermal inversion. (2) For warm, wet planets, water vapor modulates the atmospheric lapse rate from a dry adiabat towards the moist adiabat, which is likely to similarly affect the surface lapse rate for thick atmospheres. (3) For cold, wet planets, the ice-albedo feedback is important. The existence of ice would decrease absorbed solar insolation. In the optically thin limit, one would then expect to find a surface temperature discontinuity near the snowline. In the optically thick limit, our mechanism suggests that the surface lapse rate still approaches the adiabat, independent of the presence of snow or ice (which is broadly consistent with present-day Earth). (4) The influence of spectral properties of real greenhouse species (e.g., CO_2, H_2O) are ignored in this work. Even for optically thick atmospheres, the surface can still emit to space through the spectral windows in non-grey atmospheres. Different greenhouse gas emission spectra are therefore likely to affect the quantitative results, although we have found that changing optical thickness in our gray atmosphere qualitatively reproduces the effect of increasing CO_2. (5) Rayleigh scattering by atmospheric molecules (which influences shortwave heating, SW, and is related to pressure) is ignored in this paper. It was found to be unimportant within the parameter space used in our study. But the role of reflection by clouds remains unknown.

Inspired by earlier research on Mars (Forget et al., 2013; Wordsworth et al., 2013; Wordsworth, 2016; Kite, 2019), our work suggests that early Martian sedimentary geology might be explained by a new end-member option for the climate: "high T_s + non-CO_2 greenhouse gases + low P_{CO2}". Under this scenario, changes in fluvial patterns may arise from non-CO_2 greenhouse forcings rather than the loss of a CO_2-dominated atmosphere (Kite et al., 2022). The non-CO_2 greenhouse forcing could be water ice cloud radiative forcings (Urata & Toon, 2013; Kite et al., 2021), or $H_2 + CO_2$ collision-induced absorption (Wordsworth et al., 2017; Turbet & Forget, 2021). Future work should further test the correlation between river locations and elevation with non-CO_2 greenhouse forcings and low atmospheric pressure ($p_s < 1$ bar).

With respect to the habitability of exoplanets, our work also highlights the potential role of topography in creating cold traps in optically thick atmospheres, in addition to the cold traps created by radiation deficts and atmospheric circulation (Ding & Wordsworth, 2020). Most exoplanet GCMs assume no topography. However, topography allows a greater chance for water to condense. Future work could focus on different potential climate regimes under the competition of these cold traps, as well as their influences on the hydrological cycle and long-term planetary evolution (e.g., the transition between snowball and habitable climates).

Acknowledgments

This research was funded by NASA (80NSSC20K0144+80NSSC18K1476) and NSF award AGS-2033467. We thank Robin Wordsworth and an anonymous reviewer for comments that led to an improved manuscript. We also thank Tiffany Shaw for helpful discussions. Our simulations were completed with resources provided by the University of Chicago Research Computing Center (RCC). A portion of this work was carried out at the Jet Propulsion Laboratory, California Institute of Technology, under a contract with the National Aeronautics and Space Administration (80NM0018D0004).

Open Research

Data necessary to reproduce the figures in this paper is publicly available through Zenodo (https://doi.org/10.5281/zenodo.8404011) or by emailing the lead author.

References

Chow, K.-C., Xiao, J., Chan, K. L., & Wong, C.-F. (2019). Flow associated with the condensation and sublimation of polar ice caps on Mars. *Journal of Geophysical Research: Planets*, *124*(6), 1570–1580.

Cronin, T. W., & Jansen, M. F. (2016). Analytic radiative-advective equilibrium as a model for high-latitude climate. *Geophysical Research Letters*, *43*(1), 449–457.

Ding, F., & Wordsworth, R. D. (2020). Stabilization of dayside surface liquid water via tropopause cold trapping on arid slowly rotating tidally locked planets. *The Astrophysical Journal Letters*, *891*(1), L18.

Ding, F., & Wordsworth, R. D. (2021). Multiple moist climate equilibrium states on arid rocky M-dwarf planets: A last-saturation tracer analysis. *The Planetary Science Journal*, *2*(5), 201.

Forget, F., Haberle, R. M., Montmessin, F., Levrard, B., & Head, J. W. (2006). Formation of glaciers on Mars by atmospheric precipitation at high obliquity. *Science*, *311*(5759), 368–371.

Forget, F., et al. (2013). 3D modelling of the early Martian climate under a denser CO_2 atmosphere: Temperatures and CO_2 ice clouds. *Icarus*, *222*(1), 81–99.

Held, I. M. (1993). Large-scale dynamics and global warming. *Bulletin of the American Meteorological Society*, *74*(2), 228–242.

Joshi, M., Elvidge, A., Wordsworth, R., & Sergeev, D. (2020). Earth's polar night boundary layer as an analog for dark side inversions on synchronously rotating terrestrial exoplanets. *The Astrophysical Journal Letters*, *892*(2), L33.

Kamada, A., Kuroda, T., Kasaba, Y., Terada, N., & Nakagawa, H. (2021). Global climate and river transport simulations of early Mars around the noachian and hesperian boundary. *Icarus*, *368*, 114618.

Kaspi, Y., & Showman, A. P. (2015). Atmospheric dynamics of terrestrial exoplanets over a wide range of orbital and atmospheric parameters. *The Astrophysical Journal*, *804*(1), 60.

Kite, E. S. (2019). Geologic constraints on early Mars climate. *Space Science Reviews*, *215*(1), 10.

Kite, E. S., Mischna, M. A., Fan, B., Morgan, A. M., Wilson, S. A., & Richardson, M. I. (2022). Changing spatial distribution of water flow charts major change in Mars' greenhouse effect. *Science Advances*, *8*(21), eabo5894.

Kite, E. S., Steele, L. J., Mischna, M. A., & Richardson, M. I. (2021). Warm early Mars surface enabled by high-altitude water ice clouds. *Proceedings of the National Academy of Sciences*, *118*(18).

Koll, D. D., & Abbot, D. S. (2016). Temperature structure and atmospheric circulation of dry tidally locked rocky exoplanets. *The Astrophysical Journal*, *825*(2), 99.

Marinova, M. M., McKay, C. P., & Hashimoto, H. (2005). Radiative-convective model of warming Mars with artificial greenhouse gases. *Journal of Geophysical Research: Planets*, *110*(E3).

Mischna, M. A., Lee, C., & Richardson, M. (2012). Development of a fast, accurate radiative transfer model for the Martian atmosphere, past and present. *Journal of Geophysical Research (Planets)*, *117*(E10), E10009.

Mitchell, J. L., & Lora, J. M. (2016). The climate of Titan. *Annual Review of Earth and Planetary Sciences*, *44*, 353–380.

Payne, A. E., Jansen, M. F., & Cronin, T. W. (2015). Conceptual model analysis of the influence of temperature feedbacks on polar amplification. *Geophysical Research Letters*, *42*(21), 9561–9570.

Richardson, M. I., Toigo, A. D., & Newman, C. E. (2007). PlanetWRF: A general purpose, local to global numerical model for planetary atmospheric and climate dynamics. *Journal of Geophysical Research (Planets)*, *112*(E9), E09001.

Sagan, C., & Pollack, J. B. (1968). Elevation Differences on Mars. *Journal of Geophysical Research*, *73*, 1373.

Seager, S. (2013). Exoplanet habitability. *Science*, *340*(6132), 577–581.

Toigo, A. D., Lee, C., Newman, C. E., & Richardson, M. I. (2012). The impact of resolution on the dynamics of the martian global atmosphere: Varying resolution studies with the MarsWRF GCM. *Icarus*, *221*(1), 276-288.

Turbet, M., & Forget, F. (2021). 3-D Global modelling of the early Martian climate under a dense CO_2+H_2 atmosphere and for a wide range of surface water inventories. *arXiv e-prints*, arXiv:2103.10301.

Urata, R. A., & Toon, O. B. (2013). Simulations of the martian hydrologic cycle with a general circulation model: Implications for the ancient martian climate. *Icarus*, *226*(1), 229–250.

Wordsworth, R. (2015). Atmospheric heat redistribution and collapse on tidally locked rocky planets. *The Astrophysical Journal*, *806*(2), 180.

Wordsworth, R., Forget, F., Millour, E., Head, J., Madeleine, J.-B., & Charnay, B. (2013). Global modelling of the early Martian climate under a denser CO_2 atmosphere: Water cycle and ice evolution. *Icarus*, *222*(1), 1–19.

Wordsworth, R., et al. (2017). Transient reducing greenhouse warming on early Mars. *Geophysical Research Letters*, *44*(2), 665–671.

Wordsworth, R. D. (2016). The climate of early Mars. *Annual Review of Earth and Planetary Sciences*, *44*(1), 381-408.

Wordsworth, R. D., Kerber, L., Pierrehumbert, R. T., Forget, F., & Head, J. W. (2015).

Comparison of "warm and wet" and "cold and icy" scenarios for early Mars in a 3-D climate model. *Journal of Geophysical Research: Planets*, *120*(6), 1201–1219.

Yang, J., & Abbot, D. S. (2014). A low-order model of water vapor, clouds, and thermal emission for tidally locked terrestrial planets. *The Astrophysical Journal*, *784*(2), 155.

Zhang, D., & Anthes, R. A. (1982). A high-resolution model of the planetary boundary layer—sensitivity tests and comparisons with SESAME-79 data. *Journal of Applied Meteorology (1962-1982)*, 1594–1609.